Imaging G protein–coupled receptors while quantifying their ligand-binding free-energy landscape

David Alsteens[#1], **Moritz Pfreundschuh**[#1], **Cheng Zhang**[2,4], **Patrizia M Spoerri**[1], **Shaun R Coughlin**[3], **Brian K Kobilka**[2], and **Daniel J Müller**[1]

[1]Department of Biosystems Science and Engineering, Eidgenössische Technische Hochschule (ETH) Zurich, Basel, Switzerland [2]Department of Cellular Physiology and Medicine, Stanford University School of Medicine, Stanford, California, USA [3]Cardiovascular Research Institute, University of California, San Francisco, San Francisco, California, USA

[#] These authors contributed equally to this work.

Abstract

Imaging native membrane receptors and testing how they interact with ligands is of fundamental interest in the life sciences but has proven remarkably difficult to accomplish. Here, we introduce an approach that uses force-distance curve–based atomic force microscopy to simultaneously image single native G protein–coupled receptors in membranes and quantify their dynamic binding strength to native and synthetic ligands. We measured kinetic and thermodynamic parameters for individual protease-activated receptor-1 (PAR1) molecules in the absence and presence of antagonists, and these measurements enabled us to describe PAR1's ligand-binding free-energy landscape with high accuracy. Our nanoscopic method opens an avenue to directly image and characterize ligand binding of native membrane receptors.

PAR1 belongs to the class A subfamily of G protein–coupled receptors (GPCRs), serves as a cell surface receptor for thrombin, and is expressed by platelets, endothelial cells, smooth muscle cells, fibroblasts and a variety of other cell types[1–4]. Together with the coagulation cascade, PAR1 links tissue injury to cellular responses that mediate hemostasis, inflammation and repair[1]. PAR1 is activated by an unusual proteolytic mechanism. Thrombin cleaves the N-terminal exodomain of the receptor at a specific site (**Fig. 1a**), which exposes the thrombin receptor–activating peptide (TRAP). This 6-amino-acid sequence, SFLLRN, works as a tethered ligand that binds to the receptor's heptahelical

bundle, affects transmembrane movement and activates G proteins[1,2]. Once activated, these G proteins signal through various downstream pathways[5]. However, it has been difficult to quantify how tethered ligands bind PAR1. Understanding this process is likely to illuminate peptide hormone–receptor interaction as well as tethered ligand mechanisms in general, which operate in multiple GPCR types[6,7] and other biological regulators.

Force-distance curve–based atomic force microscopy (FD-based AFM) has recently matured into a nanoscopic tool that allows imaging of biological systems and simultaneous mapping of their multiple properties at nanometer or subnanometer resolution[8–10]. To achieve this, a tip mounted on an oscillating cantilever is approached and retracted from the sample for every pixel of the AFM topograph (**Fig. 1b,c** and **Supplementary Fig. 1**). The deflection of the AFM cantilever corresponds to the interaction forces between tip and sample[11] (**Fig. 1d**), which can be displayed as force-versus-time or force-versus-distance (FD) curves. Analysis of these force curves allows the extraction of parameters including adhesion, contact force, sample deformation, energy dissipation and Young's modulus[8]. Determined pixel for pixel, these parameters provide parametric maps complementing the sample topography. However, until now, FD-based AFM could not be applied to image native receptors and to quantify their mechanical, kinetic and thermodynamic binding to ligands.

Here we report an FD-based AFM approach that allowed us to image single human PAR1 molecules in proteoliposomes at high resolution (<5 nm) and to simultaneously characterize their ligand-binding energy landscape under physiologically relevant conditions. Our nanoscopic approach, combined with a new theoretical model, quantifies kinetic and thermodynamic parameters that describe the binding of PAR1 to native and synthetic ligands.

RESULTS

FD-based AFM of native PAR1 in proteoliposomes

Reconstitution of human PAR1 into proteoliposomes was confirmed by SDS-PAGE and single-molecule force spectroscopy (SMFS) (**Supplementary Figs. 2** and **3**). Unfolding single PAR1 molecules by SMFS revealed reproducible patterns indicating that all PAR1 molecules in the proteoliposomes show the same fold. Because SMFS spectra recorded upon unfolding of PAR1 closely resembled those previously recorded for the human β_2-adrenergic receptor (β_2AR)[12], a class A GPCR showing high structural homology to PAR1 (ref. 13), we concluded that PAR1 folded correctly into the proteoliposomes[14]. For FD-based AFM we imaged PAR1 proteoliposomes adsorbed onto freshly cleaved mica in buffer solution at 37 °C (**Fig. 2a**). Most of the membrane patches showed sparsely distributed protrusions, which originated from single and clustered PAR1 molecules (**Supplementary Figs. 4** and **5**).

Imaging and detecting ligand-specific interactions of PAR1

To characterize ligand binding to PAR1, we covalently linked the native PAR1 N terminus ending with the SFLLRN sequence to a poly(ethylene glycol) (PEG) spacer that was chemically attached to the AFM tip (**Fig. 1a–c**). This tethering mimicking the thrombin-

cleaved N terminus of PAR1 ensured that our experiment represents the physiologically relevant situation. Using the functionalized AFM tip, we imaged PAR1 proteoliposomes and recorded pixel-by-pixel FD curves (**Fig. 2b,c**), from which we reconstructed sample topographs (**Fig. 2d**) and adhesion maps (**Fig. 2e** and **Supplementary Figs. 6** and **7**). The retraction FD curves showed one of three characteristics (**Fig. 2c**): (i) no adhesion events, (ii) nonspecific adhesion events in the contact region (<4–5 nm) of tip and sample, or (iii) specific adhesion events distant (>5 nm) from the contact region. This distance criterion separating nonspecific from specific interactions ensures that the specific adhesion event originates from the ligand at the free end of the stretched PEG-polypeptide linker. The overlay of topography and adhesion map structurally correlated nonspecific and specific adhesion events (**Fig. 2f**). Very rarely (<0.1%, $n > 10{,}000$), FD curves detected nonspecific adhesion events on the lipid bilayer at distances within the nonspecific tip-sample contact region (<5 nm). However, no specific adhesion events were detected on membrane areas devoid of PAR1. We also observed that some PAR1 molecules did not interact with the functionalized AFM tip. As the ligand binds to the extracellular surface of PAR1 (**Fig. 1a**; ref. 15), this lack of specific binding events could have resulted from PAR1 molecules exposing their intracellular surface to the AFM tip. Alternatively, it could have been that the contact time (~1 ms) between AFM tip and proteoliposome was too short to allow ligand binding or that some PAR1 molecules resided in an inactive state[16].

Finally, some force curves detected specific adhesion events ranging from 40 to 150 pN, at rupture distances >5 nm and closely localized to receptors (<10 nm). Small divergences in colocalizing PAR1 and specific interaction occurred because the native SFLLRN ligand was tethered to the AFM stylus via a long flexible PEG spacer and the polypeptide sequence of the thrombin-cleaved N terminus of PAR1 (**Fig. 1c**). To determine whether these binding events were specific, we performed four independent controls using (i) a bare (not functionalized) AFM tip, (ii) a tip functionalized with the PEG spacer carrying the PAR1 N terminus but with the SFLLRN ligand replaced by a Gly_6 peptide, (iii) a tip functionalized with the PEG spacer carrying the PAR1 N terminus but with the SFLLRN ligand scrambled to FLLNSR and (iv) the native SFLLRN ligand–functionalized tip after blocking PAR1 with the antagonist BMS-200261 (**Supplementary Fig. 8**; ref. 17). These controls showed that bare AFM tips and Gly_6 and scrambled-sequence functionalized tips did not interact specifically with PAR1 and that the antagonist (BMS) abolished any specific interactions of the SFLLRN-functionalized AFM tip. This confirmed that the SFLLRN ligand bound to the tip could undergo specific interactions with PAR1.

In our FD-based AFM experiments, the oscillating tip touched the proteoliposomes at the end of every downward movement. Optimal conditions to detect ligand-specific interactions were found at oscillation frequencies of 0.25 kHz and amplitudes of 50 nm. Under these conditions, the contact time between the AFM tip carrying the ligand and the membrane was ~1 ms. How could the SFLLRN ligand bind PAR1 over such short time spans? In FD-based AFM the ligand is repeatedly brought in close proximity (binding radius is limited by linker length) to its protein target (PAR1), where binding is allowed for a certain time period. During this period the effective concentration of the ligand increases from infinitely low (ligand kept separated from PAR1) to molar range (ligand brought close to PAR1). At such a

high concentration, ligand binding to the receptor is not in equilibrium, thereby forcing the association of the ligand-receptor pair. Similarly, previous FD-based AFM studies have shown that contact times of ~1 ms are sufficient to enable the specific binding of Ni^{2+}-*N*-nitrilotriacetate groups held in close proximity to histidine residues[9,18]. This non-equilibrium condition, which is the native situation for the SFLLRN ligand tethered to the N-terminal end of PAR1 (**Fig. 1**; ref. 1), explains why we could measure ligand binding to PAR1 in relatively short contact times, but it also suggests that our approach could in principle force even low-affinity ligands to bind the receptor.

Approaching the free-energy landscape of the receptor

Generally, force-probing methods such as FD-based AFM measure the strength of single bonds under an externally applied force. Described by the Bell-Evans model[19,20], an external force stressing a bond reduces the activation-energy barrier toward dissociation and, hence, reduces the lifetime of the ligand-receptor pair[21,22] (**Fig. 3a**). The model predicts that far from equilibrium, the rupture force (e.g., binding strength) of the ligand-receptor bond is proportional to the logarithm of the loading rate, LR, which describes the force applied over time. Recently, Friddle, Noy and de Yoreo introduced a model to interpret the nonlinearity of the rupture forces measured over a wide range of LRs and suggested that this nonlinearity arises through the re-formation of bonds at small LRs[23]. Such bond re-formation is supported by the confining potential of the force transducer. This model provides direct access to the equilibrium free energy ΔG_{bu} between bound and unbound states (**Fig. 3a**). We therefore asked how we could use FD-based AFM to extract free-energy landscape parameters of ligand-receptor bonds.

Conventionally, to approach the free-energy landscape parameters of ligand binding to a receptor requires the acquisition of force spectra over a wide range of LRs[21,24,25]. Thus, one would have to record many FD-based AFM images of PAR1 at different velocities separating the functionalized AFM tip from the sample. However, our FD-based AFM oscillates the AFM cantilever at a fixed frequency (0.25 kHz) in a sinusoidal manner to approach and separate AFM tip and sample[8]. For an oscillation amplitude of 50 nm, the pulling velocity thus varies from approximately 0 to 80 μm s^{-1} (**Fig. 3b**). Depending at which distance (or time) of the tip movement the ligand-receptor bond ruptures, this wide range of pulling velocities applies an enormous span of LRs to the bond. The tip-sample distance of the rupture event is influenced by different factors such as the localization of the ligand on the apex of the tip, the protruding height of the receptor from the membrane, and the relative position of the ligand tethered to the tip and the receptor. Importantly, because the time period t_p stressing the bond is very brief (~0.15 ms), the pulling velocity and, thus, the LR during the rupture process can be considered constant (**Fig. 3c**). To determine the LR for each bond rupture force, we displayed the FD curve as a force-time curve (**Fig. 3d**). From this force-time curve, the LR was determined (**Fig. 3d,e**).

Determining the free-energy landscape parameters

To quantify the free-energy landscape of the SFLLRN ligand binding to native PAR1, we analyzed the specific rupture events detected by FD-based AFM. The dynamic force spectroscopy (DFS) plot showed that SFLLRN-PAR1 bonds ruptured at forces ranging from

40 to 150 pN and at LRs ranging from 4,000 to 1,100,000 pN s^{-1} (**Fig. 4a**). These rupture forces depend nonlinearly on the logarithm of the LR.

To fit the data of the DFS plot, we used the analytical approximation of the Friddle–Noy–de Yoreo model[23]:

$$\langle F \rangle \cong F_{eq} + F_{\beta}\ln\left(1 + e^{-\gamma}R\left(F_{Eq}\right)\right) \quad (1)$$

with

$$F_{\beta} = \frac{k_b T}{x_u}, \quad R\left(F_{eq}\right) = \frac{r}{k_{off}\left(F_{eq}\right)F_{\beta}} \quad \text{and} \quad F_{eq} = \sqrt{2k_{eff}\Delta G_{bu}}$$

F_{eq} is the equilibrium force for the bond-transducer system, F_{β} the thermal force, γ Euler's constant, k_b the Boltzmann constant, T the temperature and k_{eff} the effective spring constant of cantilever and linker. k_{eff} is calculated using the cantilever stiffness k_c and the PEG-polypeptide linker stiffness k_L tethering the PAR1 ligand to the AFM tip. k_L is estimated by combining the model for PEG elasticity[26] with the worm-like chain model (WLC) describing the polypeptide extension[27] (**Supplementary Fig. 9** and **Supplementary Note**). This stiffness k_{eff} of the cantilever-PEG-polypeptide linker system describes the rupture force peaks of the ligand-receptor bonds very well (**Supplementary Figs. 10** and **11**). F_{eq}, representing the lowest force required to break a bond for a given k_{eff}, has been determined by theoretical and experimental studies[28–30].

Fitting equation (1) to the DFS plot within 99% confidence and prediction intervals described the experimental data well and extracted the free-energy landscape parameters of the native ligand-receptor bond (**Fig. 4a**). We found distances from the bound state to the transition state barrier of ~0.6 Å, which is in good agreement with values determined for cell surface receptors bound to peptide-based ligands (e.g., $\alpha_2\beta_1$-integrin–binding RGD peptides)[31]. The SFLLRN ligand showed rapid dissociation rates of ~3,621 s^{-1} from PAR1, which were predicted for other ligands binding to GPCRs such as procaterol binding to human β_2AR[32]. Furthermore, the binding equilibrium free energy G_{bu} of −11.22 kcal mol^{-1} corresponds to a dissociation constant K_d of ~350 nM (using the relation $G_{bu} = k_b T \times \ln(0.018K_d)$, where 0.018 l mol^{-1} is the partial molar volume of water), which is on the same order as the EC$_{50}$ (half-maximal effective concentration) of ~800 nM found in platelet aggregation assays[33]. A K_d in this range is expected for high-affinity interactions.

We then investigated whether the FD-based AFM experiment influenced the energy landscape parameters determined. Therefore, we doubled the drive frequency oscillating the tip to 0.5 kHz (**Supplementary Fig. 12**). As expected, the forces required to rupture the ligand-receptor bond shifted toward higher LRs. This shift, however, did not change the kinetic and thermodynamic parameters estimated from fitting the rupture forces. In summary, these results highlight that FD-based AFM, combined with a new theoretical

approach, was suitable to quantify the kinetic and thermodynamic binding of a ligand to native PAR1.

Quantifying subtle differences among ligands

Next, we wanted to test whether our nanoscopic approach was sufficiently sensitive to detect differences in the free-energy landscape of different ligands binding to PAR1. PAR1 activation strongly depends on the sequence of the SFLLRN peptide, with the phenylalanine and the arginine being important for affinity[33–35]. We therefore analyzed the influence of these two residues by replacing them individually with alanine. Interestingly, substituting the arginine residue of the native SFLLRN ligand with alanine dropped the equilibrium free energy of ligand binding to -8.61 kcal mol^{-1} and reduced affinity to $K_d \approx 30$ μM (**Fig. 4b**). The DFS plot recorded using the SALLRN peptide revealed a reduced binding equilibrium free energy of -5.73 kcal mol^{-1} and low affinity of $K_d \approx 3,500$ μM for PAR1 (**Fig. 4c**). This affinity is in the typical millimolar range for nonaffinity ligands and agrees well with platelet aggregation assays detecting no response at 200 μM SALLRN[33]. These results show that substitution of phenylalanine or of arginine by alanine in the SFLLRN sequence abolished high-affinity interactions with PAR1, which is consistent with previous functional studies of PAR1 activation by SFLLRN-based peptides[33,34] and mutational studies of the SFLLRN native tethered ligand[35].

Through a systematic approach toward developing high-affinity TRAPs, Ala-Phe(p-F)-Arg-Cha-HArg-Tyr was found to have the greatest potency to bind PAR1 (ref. 36). To quantify the binding of this synthetic ligand, we attached it to the AFM tip as described (**Fig. 2**) and conducted FD-based AFM of PAR1 proteoliposomes. The DFS plot showed that the binding strengths of the synthetic ligand were much higher than those of all other ligands probed (**Fig. 4d**). Fitting the plot with the Friddle–Noy–de Yoreo model revealed that among the ligands probed, the synthetic ligand binding to PAR1 showed the highest equilibrium free energy values: $G_{bu} \approx -11.77$ kcal mol^{-1}, corresponding to an affinity of $K_d \approx 100$ nM (**Supplementary Table 1**).

Taken together, our FD-based AFM approach revealed subtle differences in the energy landscape of different ligands binding to native PAR1. Altered ligands known to have reduced function at PAR1 showed reduced binding free energy and affinity, whereas a synthetic ligand known to have higher potency showed higher binding free energy and affinity than the native TRAP ligand.

Mechanistic insights into vorapaxar inhibition of PAR1

Vorapaxar, a PAR1 antagonist, attenuates thrombin-induced platelet activation and was recently approved for secondary prevention of heart attacks and strokes[37]. Vorapaxar binds PAR1 in a shallow extracellular binding pocket composed of residues from transmembrane helices 3–7 and extracellular loops 2 and 3 (ref. 3). Although the binding site of vorapaxar is known[3], details of how vorapaxar prevents receptor activation are not understood. To this end, we measured the binding strength of the SFLLRN and the SFLLAN peptides to PAR1 blocked by vorapaxar (**Fig. 4e,f**). Surprisingly, whereas the antagonist BMS completely abolished interactions of PAR1 with SFLLRN (**Supplementary Fig. 8g,h**), vorapaxar did

not fully block these (**Fig. 4e**). Vorapaxar lowered the binding strength of SFLLRN to PAR1, raised the free energy of ligand binding by ~2.84 kcal mol^{-1} to a value of ~−8.38 kcal mol^{-1} and lowered the ligand-receptor affinity, formerly ~350 nM, to ~40 μM (**Fig. 4e**). This suggests that vorapaxar perturbs but does not completely inhibit the binding of the SFLLRN peptide to PAR1. Because PAR1 complexed with vorapaxar is functionally inhibited, this suggests that high-affinity binding of the native ligand is required to fully activate PAR1. Interestingly, the binding strength of the SFLLAN peptide to PAR1 remained nearly unchanged in the presence of vorapaxar (**Fig. 4b,f**).

Free-energy landscape of free and vorapaxar-inhibited PAR1

Using the parameters determined for ligands binding to PAR1 (**Fig. 4**), we reconstructed the free-energy landscape for each of the ligands tested (**Fig. 5a,b**). The landscapes highlight that the native SFLLRN ligand binds PAR1 at highest affinity, whereas ligands with substitutions known to decrease potency bind at lower affinity. Furthermore, the free-energy barrier separating the ligand-bound state from the unbound state is much larger for the native ligand, thereby forming a wider free-energy valley. The smaller the free energy (or affinity) stabilizing the ligand-receptor bond, the smaller this distance to the transition state and, thus, the narrower the energy valley (**Fig. 5b**). A wider energy valley can host more conformational substates than a narrower valley[38–40]. Consequently, the native ligand energetically maximizes the bound state and allows PAR1 to adopt a conformational variability higher than those allowed by the other ligands. One may speculate that this conformational variability permits the receptor to undergo structural changes to initiate signal transduction without unbinding of the ligand.

The full antagonist vorapaxar blocks PAR1 activation by SFLLRN[37]. Whether it physically occludes the SFLLRN-binding site or prevents PAR1 from accessing conformations capable of binding SFLLRN is unknown. However, FD-based AFM detected that the native SFLLRN ligand bound vorapaxar-blocked PAR1 at much lower equilibrium free energy and transition-state distance (**Fig. 5c,d**). Intriguingly, the affinity of the interaction between SFLLRN and vorapaxar-PAR1 was similar to that of the low-affinity SFLLAN peptide binding to free PAR1 (**Fig. 5a–d**). Our results thus suggest that vorapaxar prevents SFLLRN from accessing the high-affinity ligand-binding site of PAR1 (ref. 3). Furthermore, within the accuracy of our method, SFLLAN showed no change in binding affinity to vorapaxar-blocked and free PAR1. This suggests that the alternative low-affinity ligand-binding site is not blocked by vorapaxar. Because vorapaxar blocks high-affinity but not low-affinity binding of the native ligand, we suspect that PAR1 exposes at least two ligand-binding sites or states, with the high-affinity ligand binding being required to functionally activate the GPCR. Whereas the high-affinity site is sensitive to vorapaxar and to changes in the SFLLRN sequence, the alternative low-affinity binding site (or sites) appears to bind SFLLRN and SFLLAN equally well. The low-affinity site (or sites) is therefore less specific for the structure of the SFLLRN ligand and, as vorapaxar did not alter SFLLAN-binding, is not masked or occluded by the unbound and antagonist-bound conformations of the receptor. Whether the low-affinity site is involved in the physiological receptor activation is unknown. Previous studies demonstrating roles for the extracellular loops of PAR1 in tethered ligand function have led to a speculative model in which initial binding of the peptide ligand occurs

at the extracellular loops before it penetrates into the core of the receptor through a sequence of conformational intermediates[3,35]. Our observation supports such a two-step binding mechanism, in which the TRAP first binds to the superficial low-affinity binding site at the extracellular surface and then to the central high-affinity binding site toward activating PAR1 (ref. 3; **Fig. 5e**).

DISCUSSION

Although the crystal structures of PAR1 and of many other GPCRs have been solved[3,13,16,32], quantifying ligand binding to membrane receptors remains challenging. Here we introduced an FD-based AFM approach that we used to image human PAR1 molecules in proteoliposomes at high resolution and to simultaneously quantify their dynamic binding strength to different ligands. Our single-molecule method allowed us to efficiently characterize the free-energy landscape of ligands binding to PAR1 (**Fig. 4**). The sinusoidal moving AFM tip largely varies velocity, which, along with the variable elastic stiffness of the cantilever-PEG-polypeptide linker system, accounts for a wide span of LRs applied to probe the ligand-receptor bond. Such a wide span is required to explore the thermodynamic regime and to a lesser extent the kinetic regime of the bond. Currently, most commercially available FD-based AFMs, such as the one used in our study, allow users to explore only a limited range of LRs. We expect that this technological limitation will be soon largely overcome.

We see FD-based AFM as poised to become a valuable tool for the multiparametric characterization of membrane receptors. The next challenge will be to image membrane receptors at subnanometer resolution[8] and to precisely detect where and how ligands interact with the ligand-binding pocket. Another challenge is to characterize the free-energy landscape of ligands binding to single receptors showing heterogeneous distributions and functional states in native membranes. Ultimately this will guide the community toward mapping the ligand-binding free-energy landscape of single membrane receptors in cells and help uncover how receptors are regulated.

online methods

Cloning, purification, overexpression and reconstitution of PAR1

wtPAR1 was generated with an N-terminal FLAG epitope and a C-terminal His$_8$ tag to facilitate protein purification. The carboxyl terminus of PAR1 was truncated after residue Tyr397, and the amino terminus starts from residue Ala36. This construct was tested in cell-based assays to show the ability of signaling in response to thrombin activation. PAR1 expression was done in Sf9 cells (ExpressionSystems) using the pFastBac baculovirus system (Invitrogen). Cells were cultured in suspension in ESF 921 insect cell culture medium (ExpressionSystems). The cell lines were not tested for mycoplasma contamination or authenticated for these experiments. (However, after extracting the PAR1 receptors from Sf9 cells, we conducted G-protein activation assays of PAR1 receptors to prove that the receptor was able to activate G_i protein in the presence of a specific agonist. Thus, the extracted receptor was PAR1, and PAR1 was fully active.)

To purify PAR1, we lysed infected cells by osmotic shock in low-salt buffer (10 mM Tris-HCl, pH 7.5, 1 mM EDTA) containing 100 nM vorapaxar derivative and 100 µM tris (2-carboxyethyl)phosphine (TCEP). The vorapaxar derivative, generated by reducing the nonaromatic carbon-carbon double bond in vorapaxar, showed a much faster dissociation rate than that of vorapaxar in cell-based assays. PAR1 was further extracted from cell membranes with buffer: 20 mM 4-(2-hydroxyethyl)-1-piperazineethanesulfonic acid (HEPES), pH 7.5, 500 mM NaCl, 1% dodecyl maltoside (DDM), 0.03% cholesterol hemisuccinate (CHS), 0.2% sodium cholate, 15% glycerol, 100 nM vorapaxar derivative and 100 µM TCEP. Cell debris was removed by high-speed centrifugation. From this point, 1 µM vorapaxar derivative was added to all following buffers used for purification except for the buffer used in size-exclusion chromatography. Nickel-NTA agarose resin was added to the supernatant after homogenization and stirred for 1 h at 4 °C. The resin was then washed three times in batch with buffer composed of 20 mM HEPES, pH 7.5, 500 mM NaCl, 0.1% DDM, 0.02% CHS and 1 µM vorapaxar derivative and then transferred to a glass column. The bound receptor was eluted with buffer containing 300 mM imidazole and loaded onto an anti-FLAG M1 affinity column. After an extensive washing with buffer composed of 20 mM HEPES, pH 7.5, 500 mM NaCl, 0.1% DDM, 0.02% CHS, 1 µM vorapaxar derivative and 2 mM Ca^{2+}, the receptor was eluted from M1 resin using the same buffer without Ca^{2+} but with 200 µg ml^{-1} FLAG peptide and 5 mM EDTA. Size-exclusion chromatography was used to obtain the final monodisperse receptor preparation. The running buffer contained 20 mM HEPES, pH 7.5, 100 mM NaCl, 0.1% DDM and 0.02% CHS. The flow rate was set at 0.2 ml min^{-1} to give enough time to allow the vorapaxar derivative to dissociate from the receptor. The purified unliganded PAR1 was reconstituted at 10 µM n liposomes made of 0.5 mg ml^{-1} phospholipids (1,2-dioleoyl-sn-glycero-3-phosphocholine (DOPC)) and 0.05 mg ml^{-1} of the cholesterol analog CHS as described[41]. Vorapaxar-bound PAR1 was prepared in a similar way as described above except that 100 nM vorapaxar, not its derivative, was used for lysis and solubilization of cell membranes, and 1 µM vorapaxar was used in the following Nickel-NTA, anti-FLAG M1 affinity and size-exclusion chromatography steps.

Functionalization of AFM tips

To functionalize AFM tips, we used N-hydroxysuccinimide (NHS)-PEG$_{27}$-maleimide linkers[42]. High-resonance rectangular-shaped Si_3N_4 cantilevers (~0.04–0.08 N nm^{-1}, 35 kHz in water, Olympus, AC40) were immersed in chloroform for 10 min, rinsed with ethanol, dried with a stream of filtered N_2, cleaned for 10 min in a ultraviolet radiation and ozone (UV-O) cleaner (Jetlight) and immersed overnight in an ethanolamine solution (3.3 g of ethanolamine into 6.6 ml of DMSO). The cantilevers were then washed three times with DMSO and two times with ethanol and then dried with N_2. Ethanolamine-coated cantilevers were immersed for 2 h in a solution prepared by mixing 1 mg of maleimide-PEG-NHS dissolved in 0.5 ml of chloroform with 30 µl of triethylamine, then washed with chloroform and dried with N_2. 100 µl of 1 mM of peptide of interest carrying a cysteine at the C-terminal end was premixed with 2 µl of EDTA (100 mM, pH 7.5), 5 µl of HEPES (1 M, pH 7.5), 2 µl of TCEP hydrochloride (100 mM) and 2 µl of HEPES (1 M, pH 9.6). This mixture was pipetted onto the cantilevers. After 4 h of reaction, cantilevers were washed in PBS and used within a few days.

PAR1 preparation for AFM

The reconstituted PAR1 solution was 300-fold diluted in buffer solution (300 mM NaCl, 20 mM HEPES, 25 mM MgCl$_2$) and adsorbed onto freshly cleaved mica for 1 h. The sample was rinsed with the same buffer five times before AFM measurements[43]. It has been shown that after being adsorbed onto mica, human GPCRs remain stable for more than 24 h (ref. 41). This structural stability of the PAR1 sample adsorbed onto mica has been confirmed by SMFS (**Supplementary Fig. 3**). Once adsorbed onto mica, the PAR1 sample was mounted and imaged using FD-based AFM as described[10].

FD-based AFM

A Nanoscope Multimode 8 (Bruker) was operated (Nanoscope software v9.1) in the PeakForce QNM mode to conduct FD-based AFM. The AFM was equipped with a 120-μm piezoelectric scanner. Overview images (10 × 10 μm^2) were recorded at imaging forces of ~150 pN, the AFM tip was oscillated vertically at 2 kHz, applying a 30- to 50-nm amplitude, the sample was scanned using a line frequency of 1 Hz, and 512 pixels were scanned per line (512 lines). The best high-resolution AFM topographs and interaction maps showing a maximum signal-to-noise ratio and applied force errors <10 pN were obtained at imaging forces of ~150 pN, an oscillation frequency of 0.25 kHz, oscillation amplitudes from 30 to 50 nm and line-scanning frequencies 0.125 Hz. All FD-based AFM images were recorded in imaging buffer at ~27 °C. Images and force curves were analyzed using the Nanoscope analysis software v1.50 (Bruker).

Extraction of kinetics and thermodynamics parameters

Origin software (OriginLab) was used to fit the loading rate–dependent interaction forces (**Fig. 4** and **Supplementary Fig. 12**) using a nonlinear iterative fitting algorithm (Levenberg-Marquardt) along with the Friddle–Noy–de Yoreo model. Each iteration computes a chi-square value (χ^2), after which the parameter values are adjusted to reduce χ^2. When the difference between two consecutive χ^2 values computed in two successive iterations is small enough (compared with the tolerance that we fixed at 10^{-15}), we can say that the fitting procedure converged. We fixed the maximum number of iterations to 200. To look at the validity of the fit, we also checked whether the adjusted R^2 (coefficient of determination) was >0.75, and we looked at the residual plot and the Q-Q plot. Finally, we plotted the fit along with the 99% confidence intervals as well as the 99% of prediction intervals of the interaction forces. For DFS plots, the Friddle–Noy–de Yoreo model specified that in theory 60 data points are reasonable to extract the parameters; we chose to obtain at least 150 points.

Supplementary Material

Refer to Web version on PubMed Central for supplementary material.

ACKNOWLEDGMENTS

References

1. Coughlin SR. Thrombin signalling and protease-activated receptors. Nature. 2000; 407:258–264. [PubMed: 11001069]

2. Macfarlane SR, Seatter MJ, Kanke T, Hunter GD, Plevin R. Proteinase-activated receptors. Pharmacol. Rev. 2001; 53:245–282. [PubMed: 11356985]

3. Zhang C, et al. High-resolution crystal structure of human protease-activated receptor 1. Nature. 2012; 492:387–392. [PubMed: 23222541]

4. Vu TKH, Hung DT, Wheaton VI, Coughlin SR. Molecular-cloning of a functional thrombin receptor reveals a novel proteolytic mechanism of receptor activation. Cell. 1991; 64:1057–1068. [PubMed: 1672265]

5. Arora P, Ricks TK, Trejo J. Protease-activated receptor signalling, endocytic sorting and dysregulation in cancer. J. Cell Sci. 2007; 120:921–928. [PubMed: 17344429]

6. Kunishima N, et al. Structural basis of glutamate recognition by a dimeric metabotropic glutamate receptor. Nature. 2000; 407:971–977. [PubMed: 11069170]

7. Siu FY, et al. Structure of the human glucagon class B G-protein-coupled receptor. Nature. 2013; 499:444–449. [PubMed: 23863937]

8. Dufrêne YF, Martínez-Martín D, Medalsy I, Alsteens D, Müller DJ. Multiparametric imaging of biological systems by force-distance curve-based AFM. Nat. Methods. 2013; 10:847–854. [PubMed: 23985731]

9. Alsteens D, Trabelsi H, Soumillion P, Dufrêne YF. Multiparametric atomic force microscopy imaging of single bacteriophages extruding from living bacteria. Nat. Commun. 2013; 4:2926. [PubMed: 24336094]

10. Pfreundschuh M, Martínez-Martín D, Mulvihill E, Wegmann S, Müller DJ. Multiparametric high-resolution imaging of native proteins by force-distance curve–based AFM. Nat. Protoc. 2014; 9:1113–1130. [PubMed: 24743419]

11. Butt H-J, Cappella B, Kappl M. Force measurements with the atomic force microscope: technique, interpretation and applications. Surf. Sci. Rep. 2005; 59:1–152.

12. Zocher M, Fung JJ, Kobilka BK, Müller DJ. Ligand-specific interactions modulate kinetic, energetic, and mechanical properties of the human β2 adrenergic receptor. Structure. 2012; 20:1391–1402. [PubMed: 22748765]

13. Venkatakrishnan AJ, et al. Molecular signatures of G-protein-coupled receptors. Nature. 2013; 494:185–194. [PubMed: 23407534]

14. Zocher M, Bippes CA, Zhang C, Müller DJ. Single-molecule force spectroscopy of G-protein-coupled receptors. Chem. Soc. Rev. 2013; 42:7801–7815. [PubMed: 23799399]

15. Coughlin SR. How the protease thrombin talks to cells. Proc. Natl. Acad. Sci. USA. 1999; 96:11023–11027. [PubMed: 10500117]

16. Kobilka BK, Deupi X. Conformational complexity of G-protein-coupled receptors. Trends Pharmacol. Sci. 2007; 28:397–406. [PubMed: 17629961]

17. Bernatowicz MS, et al. Development of potent thrombin receptor antagonist peptides. J. Med. Chem. 1996; 39:4879–4887. [PubMed: 8960546]

18. Pfreundschuh M, Alsteens D, Hilbert M, Steinmetz MO, Müller DJ. Localizing chemical groups while imaging single native proteins by high-resolution atomic force microscopy. Nano Lett. 2014; 14:2957–2964. [PubMed: 24766578]

19. Bell GI. Models for the specific adhesion cells to cells. Science. 1978; 200:618–627. [PubMed: 347575]

20. Evans E, Ritchie K, Merkel R. Sensitive force technique to probe molecular adhesion and structural linkages at biological interfaces. Biophys. J. 1995; 68:2580–2587. [PubMed: 7647261]

21. Evans E, Ritchie K. Dynamic strength of molecular adhesion bonds. Biophys. J. 1997; 72:1541–1555. [PubMed: 9083660]

22. Evans E. Energy landscapes of biomolecular adhesion and receptor anchoring at interfaces explored with dynamic force spectroscopy. Faraday Discuss. 1998; 111:1–16.

23. Friddle RW, Noy A, De Yoreo JJ. Interpreting the widespread nonlinear force spectra of intermolecular bonds. Proc. Natl. Acad. Sci. USA. 2012; 109:13573–13578. [PubMed: 22869712]

24. Moy VT, Florin EL, Gaub HE. Intermolecular forces and energies between ligands and receptors. Science. 1994; 266:257–259. [PubMed: 7939660]

25. Dudko OK, Hummer G, Szabo A. Theory, analysis, and interpretation of single-molecule force spectroscopy experiments. Proc. Natl. Acad. Sci. USA. 2008; 105:15755–15760. [PubMed: 18852468]

26. Sulchek T, Friddle RW, Noy A. Strength of multiple parallel biological bonds. Biophys. J. 2006; 90:4686–4691. [PubMed: 16581843]

27. Bustamante C, Marko JF, Siggia ED, Smith S. Entropic elasticity of lambda-phage DNA. Science. 1994; 265:1599–1600. [PubMed: 8079175]

28. Evans E. Probing the relation between force—lifetime—and chemistry in single molecular bonds. Annu. Rev. Biophys. Biomol. Struct. 2001; 30:105–128. [PubMed: 11340054]

29. Seifert U. Dynamic strength of adhesion molecules: role of rebinding and self-consistent rates. Europhys. Lett. 2002; 58:792–798.

30. Friddle RW, Podsiadlo P, Artyukhin AB, Noy A. Near-equilibrium chemical force microscopy. J. Phys. Chem. C. 2008; 112:4986–4990.

31. Li F, Redick SD, Erickson HP, Moy VT. Force measurements of the α_5-β_1 integrin-fibronectin interaction. Biophys. J. 2003; 84:1252–1262. [PubMed: 12547805]

32. Rosenbaum DM, et al. Structure and function of an irreversible agonist-β_2 adrenoceptor complex. Nature. 2011; 469:236–240. [PubMed: 21228876]

33. Vassallo RR Jr. Kieber-Emmons T, Cichowski K, Brass LF. Structure-function-relationships in the activation of platelet thrombin receptors by receptor-derived peptides. J. Biol. Chem. 1992; 267:6081–6085. [PubMed: 1313429]

34. Scarborough RM, et al. Tethered ligand agonist peptides. Structural requirements for thrombin receptor activation reveal mechanism of proteolytic unmasking of agonist function. J. Biol. Chem. 1992; 267:13146–13149. [PubMed: 1320011]

35. Nanevicz T, et al. Mechanisms of thrombin receptor agonist specificity. Chimeric receptors and complementary mutations identify an agonist recognition site. J. Biol. Chem. 1995; 270:21619–21625. [PubMed: 7665575]

36. Feng DM, et al. Development of a potent thrombin receptor-ligand. J. Med. Chem. 1995; 38:4125–4130. [PubMed: 7562949]

37. Morrow DA, et al. Vorapaxar in the secondary prevention of atherothrombotic events. N. Engl. J. Med. 2012; 366:1404–1413. [PubMed: 22443427]

38. Frauenfelder H, Sligar SG, Wolynes PG. The energy landscapes and motions of proteins. Science. 1991; 254:1598–1603. [PubMed: 1749933]

39. Wolynes PG, Onuchic JN, Thirumalai D. Navigating the folding routes. Science. 1995; 267:1619–1620. [PubMed: 7886447]

40. Onuchic JN, Wolynes PG, Luthey-Schulten Z, Socci ND. Toward an outline of the topography of a realistic protein-folding funnel. Proc. Natl. Acad. Sci. USA. 1995; 92:3626–3630. [PubMed: 7724609]

41. Zocher M, Zhang C, Rasmussen SGF, Kobilka BK, Müller DJ. Cholesterol increases kinetic, energetic, and mechanical stability of the human β_2-adrenergic receptor. Proc. Natl. Acad. Sci. USA. 2012; 109:E3463–E3472. [PubMed: 23151510]

42. Wildling L, et al. Linking of sensor molecules with amino groups to amino-functionalized AFM tips. Bioconjug. Chem. 2011; 22:1239–1248. [PubMed: 21542606]

43. Müller DJ, Engel A. Atomic force microscopy and spectroscopy of native membrane proteins. Nat. Protoc. 2007; 2:2191–2197. [PubMed: 17853875]
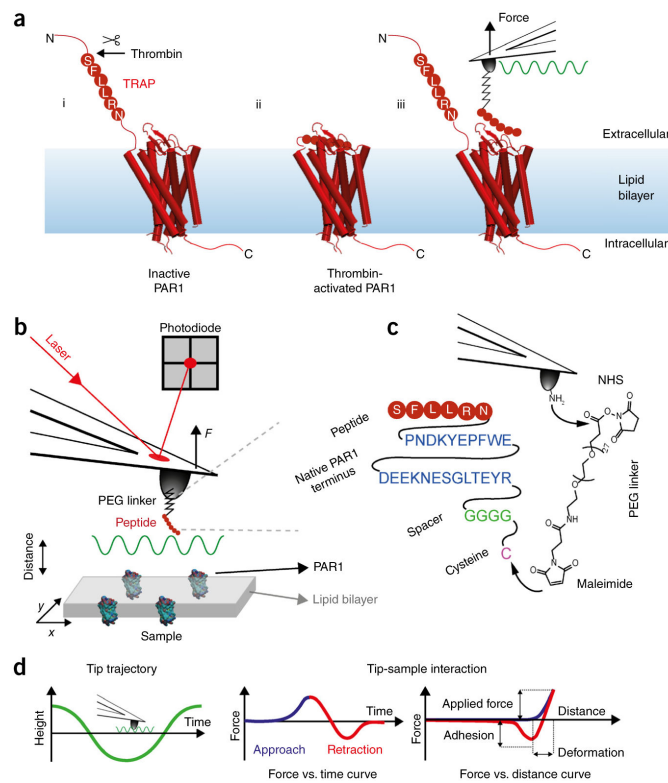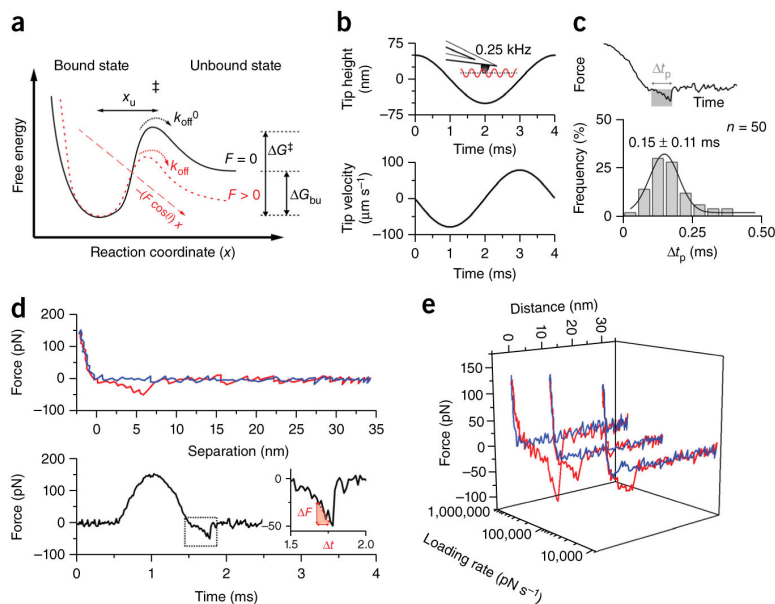
Figure 1.
Principle of FD-based AFM to detect ligand binding to PAR1. (**a**) (i) PAR1 reconstituted in a lipid bilayer. Thrombin cleaves the N-terminal domain of the GPCR and exposes the SFLLRN sequence of the cleaved N terminus. This SFLLRN sequence functions as a tethered ligand and binds to PAR1 (ii). Once the ligand has bound to PAR1, the receptor is activated and initiates transmembrane signaling. (iii) Using an AFM tip derivatized with the N-terminal SFLLRN sequence to detect interaction forces with PAR1. PAR1 structure (PDB ID 3VW7) is taken from ref. 3. (**b**) Pixel-for-pixel FD-based AFM approaches and retracts the tip of an AFM cantilever from the sample to record interaction forces *F* over the tip-sample distance in FD curves (see also **supplementary Fig. 1**). Therefore, the cantilever is oscillated in the kilohertz range (green curve). (**c**) AFM tip functionalized with a PEG spacer fused to the polypeptide of the native PAR1 terminus ending with the SFLLRN sequence. In follow-up experiments we replaced the SFLLRN sequence with various hexapeptides. (**d**) The sinusoidal movement of the cantilever allows intermittent contact of the tip with the sample. The recorded tip-sample interactions are displayed as force-time or force-distance curves. Sample properties (adhesion, deformation) can be extracted from individual force curves[8].
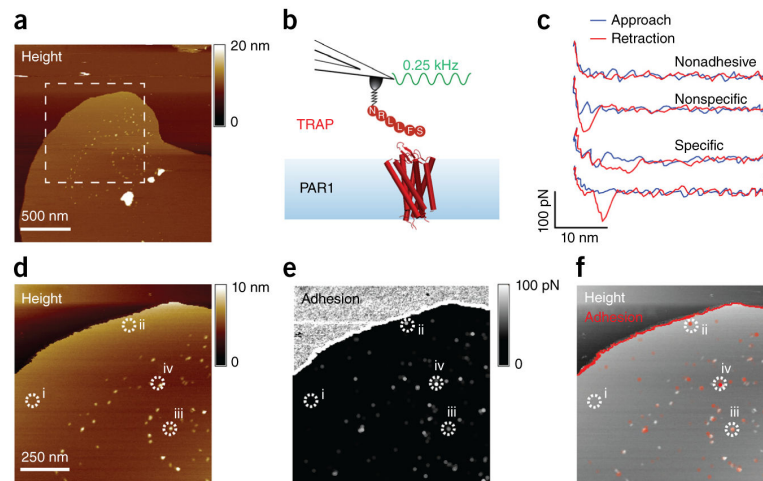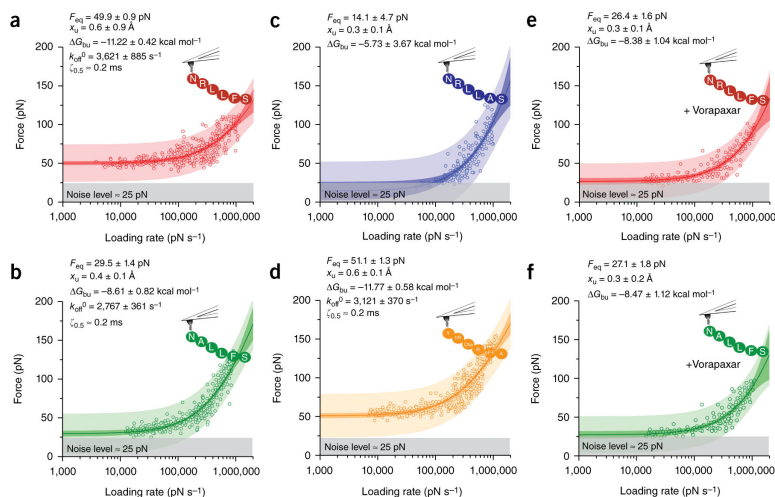
Figure 2.
Mapping ligand binding to human PAR1 using FD-based AFM. (**a**) Overview topography (height image) of human PAR1 reconstituted in liposomes made of 0.5 mg ml^{-1} phospholipids (DOPC) and 0.05 mg ml^{-1} of the cholesterol analog cholesteryl hemisuccinate (CHS) (Online Methods). (**b**) The topograph in **a** was taken with the SFLLRN ligand–functionalized AFM tip oscillated at 0.25 kHz and amplitudes of 50 nm. The membrane patches protruded 4.5 ± 0.7 nm (average ± s.d., $n = 10$) from the mica substrate (see **supplementary Fig. 4**). TRAP, thrombin receptor–activating peptide. (**c**) Representative force-distance curves recorded between the tip and the PAR1 proteoliposome. (**d,e**) Topograph (**d**) and adhesion map (**e**) of the boxed area in **a**. For visibility, adhesion pixels were enlarged 4× (**e**). (**f**) Overlay of adhesive interactions (red) with a representative AFM topograph (gray). Dashed circles and numbers localize force curves recorded in **c**. Similar results were obtained in 10 independent experiments. Other examples of topographs and adhesion maps are shown in **supplementary Figure 7**.
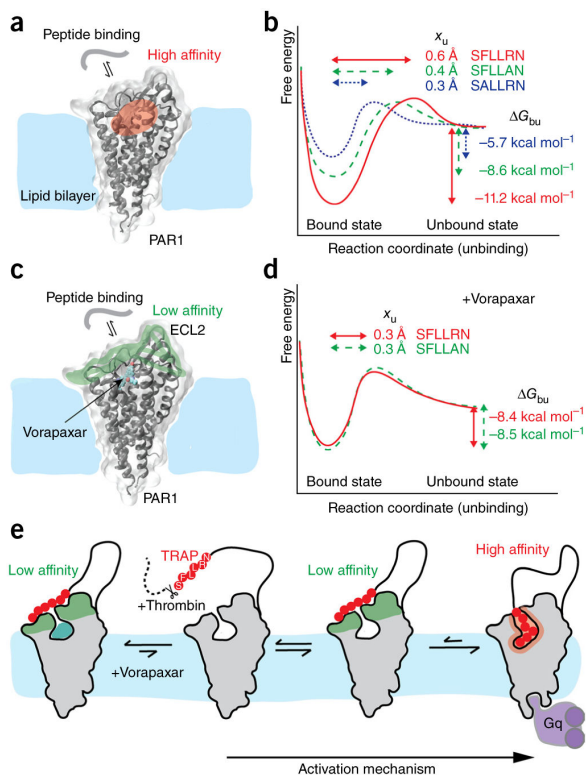
Figure 3.
Extracting energetic, thermodynamic and kinetic parameters from force curves describes the ligand-binding free-energy landscape. (**a**) According to the Bell-Evans model[21], a ligand-receptor bond can be described using a simple two-state model. The bound state resides in an energy valley and is separated by an energy barrier from the unbound state. The transition state (‡) must be overcome to separate ligand and receptor. x_u represents the distance between bound state and transition state, k_{off}^0 and k_{off} are transition rates for crossing the energy barrier under zero force and applied force F, respectively. $\Delta G^{\ddagger}$ gives the activation free energy to cross the transition state and ΔG_{bu} the free-energy difference between bound and unbound state. (**b**) Oscillation of the tip with an amplitude of 50 nm and a frequency of 0.25 Hz induces a variation in the tip height (top) with a nonconstant tip velocity (bottom). (**c**) Because the time period (Δt_p) stressing the bond until it ruptures is very brief (0.15 ± 0.11 ms; mean ± s.d.), the speed of the tip during Δt_p, and thus the loading rate, can be considered constant. n gives the number of rupture events analyzed; values are binned by 0.05 ms. (**d**) A force-distance curve can be displayed as a force-time curve, from which the loading rate can be extracted via the slope of the curve just before bond rupture (LR = $\Delta F/\Delta t$). (**e**) Representative force-distance curves (from $n > 1,000$ force curves) recorded at different loading rates.

Figure 4.

Loading rate–dependent interaction forces of single ligand-receptor bonds quantitate the ligand-binding energy landscape of PAR1. (**a**–**d**) For four different peptides SFLLRN (**a**), SFLLAN (**b**), SALLRN (**c**), and A(pF-F)RChahRY (**d**), the force required to separate the ligand from PAR1 is plotted against the loading rate. (**e**,**f**) For SFLLRN (**e**) and SFLLAN (**f**), the force required to separate the ligand from PAR1 complexed with the antagonist vorapaxar is given. Each DFS plots contain more than 300 (**a**–**d**) or 150 (**e**,**f**) measurements. Fitting the data using the Friddle–Noy–de Yoreo model (thin lines)[23] provides average F_{eq}, x_u, G_{bu}, k_{off}^0 and residence time ($\zeta_{0.5}$) values with errors representing the s.e.m. Values showing an s.e.m. two times higher than the average values are not given. Each circle represents one measurement. Darker shaded areas represent 99% confidence intervals, and lighter shaded areas represent 99% of prediction intervals.

Figure 5.

Free-energy landscape describing the thermodynamic (ΔG_{bu}) and kinetic (x_u) parameters of peptide-based ligands binding to PAR1. (**a**) Cartoon showing a peptide-based ligand binding to PAR1 through a high-affinity binding site, which is expected to be in the region shaded red[3]. (**b**) Free-energy binding landscape of three different peptide-based ligands depends on the sequence of the peptide. x_u represents the distance to the transition state separating the ligand-bound and unbound state and is indicated for each peptide by horizontal arrows. ΔG_{bu} gives the free-energy difference between the ligand-bound and unbound states and is indicated for each peptide by vertical arrows. (**c**) Cartoon showing a peptide-based ligand interacting to vorapaxar-bound PAR1 through a low-affinity binding site, which is expected to be in the region shaded green. (**d**) Free-energy landscape of ligands binding to vorapaxar-bound PAR1. PAR1 structures are shown in the vorapaxar-bound state (PDB ID 3VW7). (**e**) Binding model of the native SFLLRN ligand (red) to PAR1. For both the vorapaxar-inhibited and unbound states of PAR1, the ligand binds at low affinity to the extracellular PAR1 surface, from which extracellular loops 2 and 3 have been proposed to bind the ligand[3]. In the presence of the antagonist vorapaxar, the native ligand cannot bind to the high-affinity binding site (or state). In the absence of vorapaxar, the native ligand can bind the high-affinity site; this functionally activates PAR1, leading to the binding of Gq, a class of G proteins that participate in a variety of cellular signaling pathways.